The specific behavior of MxTiS2 (x=1/4, M=Fe, Ni) surfaces probed by scanning microscopy (STM and AFM)

Yann Tison, Hervé Martinez, Isabelle Baraille, Michel Loudet, Danielle Gonbeau

Available online at www.sciencedirect.com
SCIENCE DIRECT®
Chemical Physics 290 (2003) 267–278
Chemical Physics
www.elsevier.com/locate/chemphys

The specific behavior of M_xTiS_2 ($x = 1/4$, M = Fe, Ni) surfaces probed by scanning microscopy (STM and AFM)

Y. Tison, H. Martinez, I. Baraille*, M. Loudet, D. Gonbeau

Université de Pau et des Pays de l'Adour/UFR Sciences et Techniques, LCTPCM/CNRS UMR5624, BP 1155, 64013 Pau Cedex, France

Received 10 December 2002; in final form 11 March 2003

Abstract

The scanning tunneling microscopy (STM) and atomic force microscopy (AFM) images of two model systems $M_{1/4}TiS_2$ (M = Fe, Ni) were interpreted on the basis of the partial electron density $\rho(r, E_F)$ and total electron density $\rho(r)$ of a slab which consists of seven (0 0 1) $M_{1/4}TiS_2$ atomic layers. The geometrical structure of the slabs investigated was optimized. Electronic structure calculations were performed using the ab initio periodic LCAO-DFT method. The top sulfur plane (0 0 1) imaged gives a different answer depending both of the compounds considered and the scanning probe microscopic instrument used. Theoretical calculations have then been carried out in order to improve our knowledge of the surface electronic structure of these inserted compounds and attempts are made to rationalize the experimental data. A specific behavior of the surface electronic structure in comparison with the 3D compounds (depending on the guest specie inserted) is shown.

Keywords: Density functional calculations; Ab initio quantum chemical calculations; Scanning tunneling microscopy; Atomic force microscopy

1. Introduction

For the last years, numerous studies have been devoted to the insertion phenomena in transition metal dichalcogenides such as TX_2 (T = Ti, Mo, Ta, V and X = S, Se, Te). These compounds have layered structures with van der Waals gap, which is advantageous to insert various atoms or molecules to modify the physical properties of the host material. In particular, insertion of 3d transition-metal M into the van der Waals gap gives M_x TX_2 compounds ($0 < x < 1$).

As titanium disulfide TiS_2 is considered as the prototypal compound in the series of the TX_2 layered materials, the intercalated compounds M_xTiS_2 have been the subject of several studies [1–5]. They have been devoted predominantly to the electronic and structural modifications induced by the insertion of the transition metal. Recently, we have undertaken the analysis of the electronic structures of $M_{1/4}TiS_2$ intercalated compounds (M = Fe, Co or Ni) using both X-ray photoelectron

* Corresponding author. Present address: LCTPCM, IFR, rue Jules Ferry, 64000 Pau, France. Tel.: +33-55-972-2063; fax: +33-55-980-3769.
E-mail address: isabelle.baraille@univ-pau.fr (I. Baraille).

0301-0104/03/$ - see front matter
doi:10.1016/S0301-0104(03)00148-4

spectroscopy (XPS) and scanning tunneling microscopy (STM) [6]. This stoichiometry ($x = 1/4$) leads to specific crystallographic features, especially different sites for sulfur (mono- or bimetallic chemical surroundings) and titanium atoms. The most striking results have been obtained concerning the role played by chalcogen atoms, which is rarely considered in the literature. For example, XPS S2p core spectra are found to depend strongly to their chemical surrounding (Ti or Ti and M) and on the nature of the guest metal. Band structure calculations (FLAPW method) were also used to understand the change of the bulk electronic properties, the bonding nature between the guest atoms and the host, and are consistent with the evolution of the XPS data. STM experimental results on $M_{1/4}TiS_2$ (M = Fe, Ni) compounds have also shown different behavior according to the nature of the guest metal inserted, but no theoretical approach has been undertaken.

The purpose of this work is to understand both scanning tunneling and atomic force microscopic images, through a comparison of 2D electronic properties of $M_{1/4}TiS_2$ compounds for M = Ni and Fe. In this way, 2D theoretical calculations have been carried out with the periodic ab initio density functional method using atomic valence-electron basis sets (LCAO-DFT), developed in the CRYSTAL98 code [7,8]. The geometrical structure of the slabs investigated in this work has been optimized and the density of states analyzed in the energetic range corresponding to our experimental conditions (for 0.3 eV below the Fermi level in STM and the total valence electron density in AFM). An attempt to simulate images is realized by computing the electron density map above the plane of the top sulfur layer. Analyses of density of states, atomic valence populations, dipole and quadrupole moments along the direction perpendicular to the surface are made to improve our knowledge of the surface electronic structure of $M_{1/4}TiS_2$.

2. Experimental and computational details

The elements Fe (Co, Ni), Ti and S were mixed in appropriate proportion and placed within a quartz tube, which was sealed under vacuum. The mixture was then heated to 1050 °C (gradient 50 °C) during 10 days and afterwards slowly cooled down to room temperature. An intermediate crushing of the product was necessary to obtain homogeneity. A small amount of iodine was then added to favor crystallization [9]. The obtained single crystals were in platelet shape and could be easily cleaved. Chemical composition and phase purity were carried out with an electron microprobe (for the bulk) mounted on a scanning electron microprobe and by XPS for the surface (deduced from the intensities of the relevant XPS peaks: Ni 2p, S 2p, and Ti 2p).

We briefly remind the experimental STM results and present the AFM ones. All the STM images of the inserted compounds top sulfur planes (0 0 1) do not depend on the polarization sign. Excellent atomic resolution was obtained using −300 to 300 mV bias voltage and 0.1–3 nA tunneling current.

For $Ni_{1/4}TiS_2$, we notice two kinds of hexagonal structures (Fig. 1(a)) with lattices spacing of $2a$ and a (where $a \approx 3.4$ Å is the unit cell parameter of TiS_2). They are respectively represented by bright (25% of the image) and dark (75% of the image) spots. The Fourier transform and the height profiles, which exhibit two atom types, with different depths, confirm these two kinds of hexagonal structure. These results are in agreement with the crystallographic structure (different sulfur chemical environment in the inserted compound). We can distinguish on the $Ni_{1/4}TiS_2$ image two different and alternated atom rows: one is composed by similar brightness spots and the other alternates bright and dark dots. Furthermore, dark triangular shape zones are periodical all over the image; the unit cell seems to be formed by two triangular zones with different brightness.

The STM scans for $Fe_{1/4}TiS_2$ (Fig. 1(b)) show a unique sulfur atom hexagonal structure, with lattice spacing of 3.5 ± 0.1 Å, similar to TiS_2. The image exhibits bright and dark zones with no specific symmetry or periodicity. No commensurate or ordered superstructure is observed. These zones could be due to non-equivalent electrostatic forces, which partially carry out the cohesion between planes and lead to a non-perfect flat surface.

Thus, depending on the guest species inserted STM analysis exhibit one or two types of sulfur

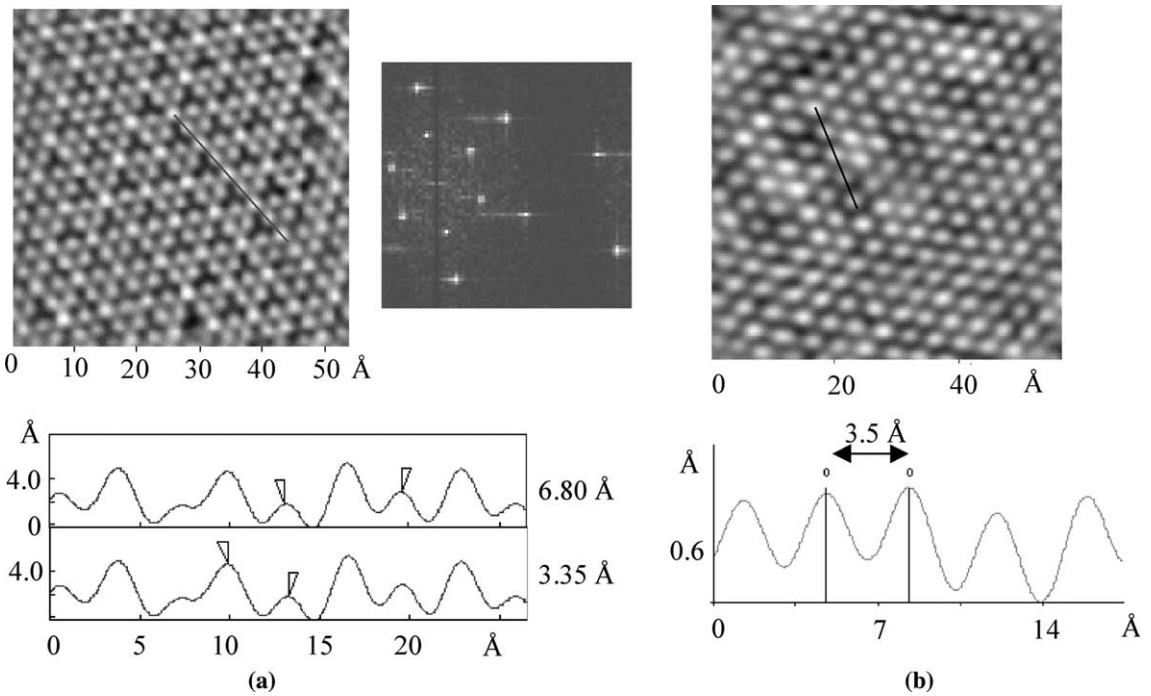

Fig. 1. STM images and associated height profiles of $Ni_{1/4}TiS_2$ (a) and $Fe_{1/4}TiS_2$ (b).

atoms. Note that it could be surprising that the sulfur atoms expected with the highest total electronic density [10] appear like dark spots in the image, while bright spots are characteristic of sulfur atoms with the lowest total electronic density. A specific electronic behavior is then expected for the outermost layer composed by chalcogen atoms.

The AFM images (Figs. 2(a) and (b)) only show a coplanar 1×1 pattern typical of native TiS_2. The force applied to the tip was the lower as possible in order to avoid frictional forces induced by the contact between the cantilever and the substrate. All spots show the same contribution to the registered signal, according to the structure of our compounds where the top layer consists on sulfur atoms. The lattice parameter (3.4 ± 0.1 Å) is in good agreement with the crystallographic structure of (0 0 1) $M_{1/4}TiS_2$ plane.

All the calculations were performed using the periodic ab initio code CRYSTAL98 developed in Turin [7,8]. The crystalline orbitals are expanded in terms of localized atomic Gaussian basis set, in a way close to the LCAO (linear combination of atomic orbitals) method currently adopted for molecules. The eigenvalues equations are solved at the B3LYP level. The hybrid B3LYP functional uses the Becke's exchange [11] and Lee–Yang–Parr's correlation functional [12]. The number of k points in the first irreducible Brillouin zone at which the Hamiltonian matrix is diagonalized was equal to 26 for both compounds. In order to reduce the computational cost, the Durand and Barthelat effective core pseudopotentials [13] were used to model the core electrons of titanium, iron, nickel and sulfur atoms. Valence basis sets already optimized in early studies were adopted (PS-141G for titanium [14], PS-2141G for nickel [15] and iron [15] and PS-3-1G for sulfur [16]). In the present work, the CRYSTAL98 code is linked to an optimization code (PENTE) [17] developed in our laboratory, which carries out the numerical optimization of any parameter (geometrical parameters or basis set exponents) relative to the total energy of the system (Newton–Raphson method).

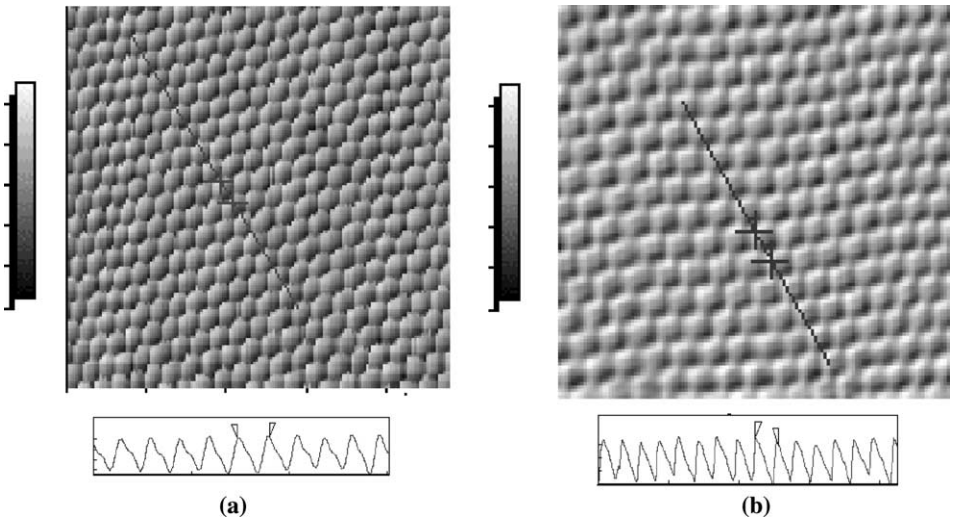

Fig. 2. AFM images and associated height profiles of $Ni_{1/4}TiS_2$ (a) and $Fe_{1/4}TiS_2$ (b).

In order to interpret the AFM and STM experimental images, we investigate the structural and electronic properties by simulating the $M_{1/4}TiS_2$ (0 0 1) surfaces by the slab model. Our slab model includes seven monoatomic layers, sulfur atoms being left at the top as shown in Fig. 3.

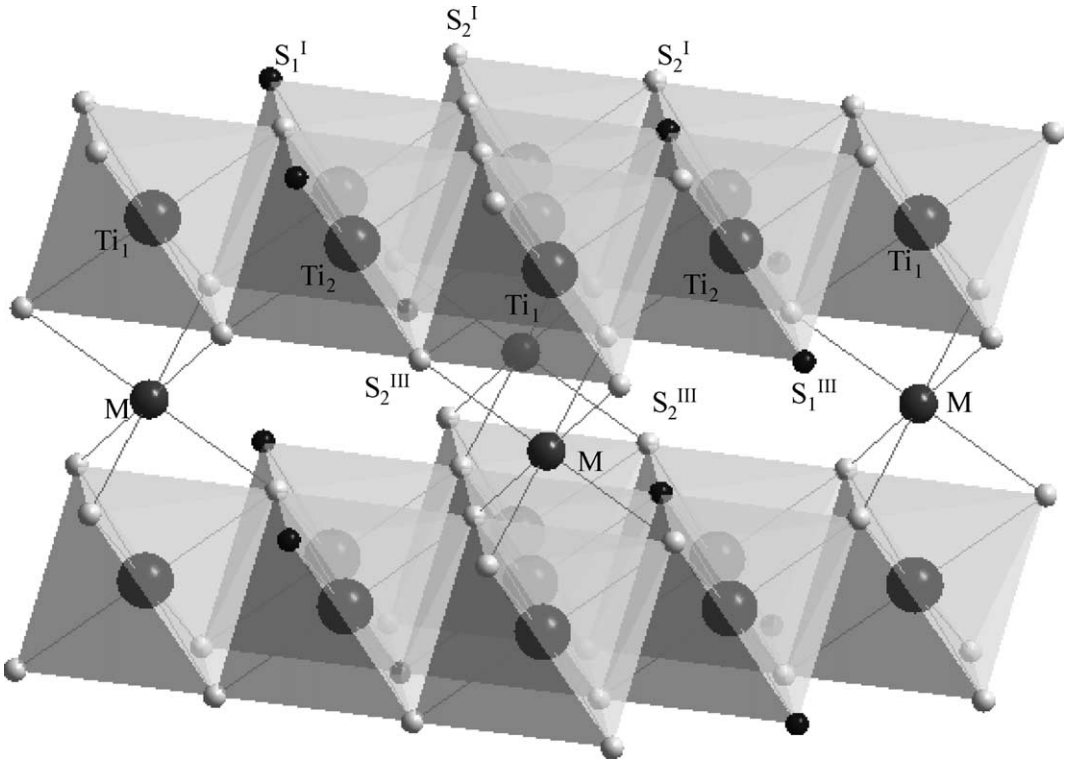

Fig. 3. Octahedral model for the $M_{1/4}TiS_2$ slab.

The bidimensional hexagonal unit cells ($P_{\bar{3}}$ layer group) are built from the experimental lattice parameters of the bulk ($P\bar{3}m1$ with $a = 6.764$ Å and $c = 5.678$ Å for M = Ni and $a = 6.836$ Å and $c = 5.708$ Å for M = Fe [1,2,18]). In the second layer, one of the titanium atoms (Ti_1) plumbs with nickel metal atom and the three others (noted Ti_2) are below or above the empty octahedral site of the van der Waals gap. There are four types of sulfur atoms: those on the top of the slab are only differentiated by their fifth neighbors: three sulfurs atoms (fifth atomic layer) for S_1^I and one metal atom for S_2^I; in the third layer, S_2^{III} atoms are coordinated to both metal and titanium atoms while S_1^{III} are only surrounded by titanium atoms.

3. Theoretical aspects to simulate STM and AFM images

The analysis of electronic properties of (0 0 1) $M_{1/4}TiS_2$ plane (which is the cleavage plane of our compound), associated with geometry optimization for a slab which consist of seven layers, will allow us to propose in a first approximation a model of our images. We can remind that at relatively small bias voltage (in agreement with our experimental conditions), and when the tip to surface interaction is negligible, the nature of the observed STM image is determined by two factors: a geometrical factor, originating from the exponential decrease of atomic orbital amplitude with distance, and an electronic factor. This last parameter is specified by the local density of filled or empty (according to the polarization, negative and positive, respectively) states at the Fermi level. Because the contribution of the subsurface atoms (titanium) or inserted species influenced the filled or empty states at the Fermi level, interpretation requires a theoretical (electronic and geometric) approach to determine the relative contribution of all atoms from the slabs to the main features of the STM images.

In atomic force microscopy (AFM), long-range attractive van der Waals forces and short-range repulsive forces, resulting from the charge overlap between the tip and the surface, act on the AFM cantilever. In the contact mode of operation, which was employed in our study, the repulsive forces thereby giving rise to the image contrast of the surface primarily cause the deflection of the cantilever. A brighter spot of the AFM image is related to a stronger repulsive force the tip feels, a greater charge overlap the tip makes with the surface, and hence a higher electron density region of the surface. Thus, the profiles of the inter atomic repulsive forces (where all electrons of the sample are involved) registered by AFM are expected to reproduce the topography of surface atoms.

Therefore, to a first approximation, the STM and AFM images are, respectively, described by the spatial electron density $\rho(r, E_F)$ and $\rho(r)$ of the sample (where r is the tip to surface distance) which simulate ideal images expected in the absence of the tip sample interactions. STM and AFM images of numerous layered or not materials [19] were successfully analyzed on the basis of calculated $\rho(r, E_F)$ and $\rho(r)$ plots calculated. Note that in STM, the origin of layered transition-metal dichalcogenide images remains controversial in terms of the role played by the different types of atoms. Considering only the electronic density surrounding the Fermi level, images in positive and negative polarization should represent the structure formed by both chalcogen and metal atoms. However, when the layered structure is considered, metal atoms are 1.5 Å apart the sulfur ones. In terms of the tip, we have shown by experimental and theoretical works [20] conducted on the mother compound TiS_2 that the titanium atoms are too far to participate in the tunneling current and so, only the plane of sulfur atoms is responsible for the image obtained.

4. Theoretical results and discussion

4.1. Geometry optimization and surface relaxation

In the optimization method, the vertical coordinates of the different atoms have been taken into account as an essential part of the relaxation phenomena occurring at the surface. More particularly these parameters could have an appreciable influence on the STM images, as this

instrument is very sensitive to the distance between the tip and the surface. The contact mode in Atomic Force Microscopy leads to minimize small geometrical variations but it is still necessary to know the altitudes of the top layer sulfur atoms. The corresponding coordinates of the six non-equivalent atoms (see Fig. 3) in the unit cell have been simultaneously optimized using the PENTE program linked to the CRYSTAL98 code [17], the metal layer being taken as a reference. To visualize the interlayer relaxation, the altitudes of the different atoms in the relaxed slab compared to the heights of the atomic planes in the unrelaxed slabs are reported in Fig. 4.

Note that concerning surface relaxation, an atom from the top plane has only neighbors in the same plane and in the underneath one. Compared to an atom from the bulk, it lacks a bonding force in the normal direction z. Then, we can expect that the last atomic planes are moved in this direction. For example, the interlayer distances evaluated from the average positions of the corresponding atoms show a contraction of the two first atomic planes by about 3% and 0.3%, respectively, for $Fe_{1/4}TiS_2$ and $Ni_{1/4}TiS_2$ and an expansion of the two following ones by about 7% and 1% (respectively for $Fe_{1/4}TiS_2$ and $Ni_{1/4}TiS_2$). The different order of magnitude for both compounds has a great effect over bond overlap populations depending on the guest species inserted and on electronic surface properties. These phenomenons are discussed below. More precisely and concerning the top anionic plane directly responsible of our experimental results, both S_1^I and S_2^I atoms have almost the same coordinates in $Fe_{1/4}TiS_2$. In the case of $Ni_{1/4}TiS_2$, the S_1^I atoms move away outwards the top layer by 0.05 Å compared to the S_2^I ones.

It could be now interesting to link geometrical optimization to bond overlap population and compared with the 3D characteristics of our compounds (Table 1). In the $Fe_{1/4}TiS_2$ slab, the Ti_1–S_2^{III} bond population (0.086 e^-) becomes weaker respective to the Ti_1–S_2 bond in the bulk (0.116 e^-) in relation with the corresponding increasing distance by 0.133 Å (note that S_2 and S_1 are relative to sulfur atoms in bi- and monometallic environments, in the bulk). On the other hand, the decreasing of the Ti_1–S_2^I distances (−0.150 Å) has to be connected with the increase of the corresponding bond overlap population (0.169 e^-) respective to the 3D compound (0.116 e^-). The Ti_2–S_2^{III} and Ti_2–S_2^I bond populations are less affected by the transition to the slab (+0.124 and +0.118 e^- instead of 0.115 e^- for the 3D system), the difference between the corresponding distances being less modified (+0.026 and +0.004 Å, respectively). The Ti_2–S_1^I and Ti_2–S_1^{III} bond populations (0.133 e^- and 0.130 e^-) have almost the same value as the Ti_2–S_1 in the bulk (0.134 e^-) or in TiS_2 (0.133 e^-) [10]. The same comments are available for $Ni_{1/4}TiS_2$ slab but the variations of the bond overlap populations are less important. In all cases (2D and 3D

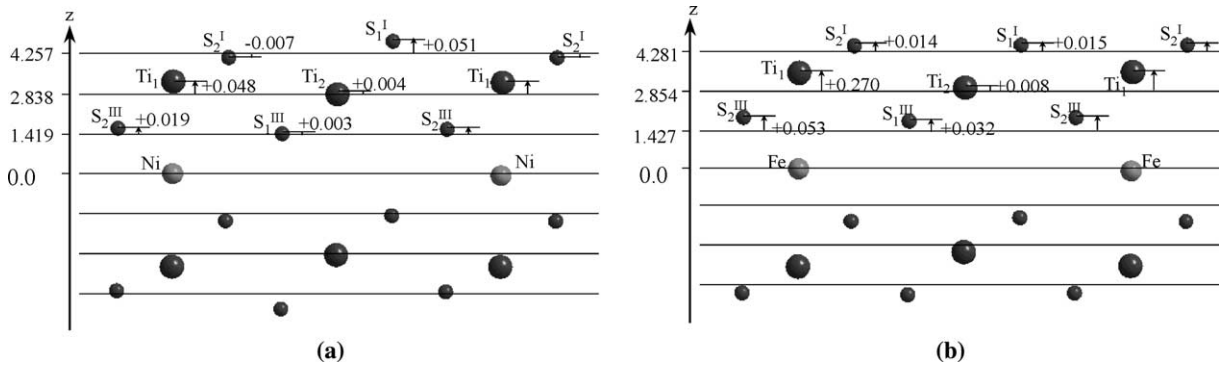

Fig. 4. Schematic optimized altitudes of the different atoms compared to the heights of the atomic planes in the unrelaxed slabs (on the z-axis) in (1 1 0) planes for $Ni_{1/4}TiS_2$ (a) and $Fe_{1/4}TiS_2$ (b). All values are given in Å.

Table 1
Total atomic valence charges and bond overlap population resulting from a Mulliken population analysis in $Fe_{1/4}TiS_2$ and $Ni_{1/4}TiS_2$ both bulk and slab. The corresponding bond lengths (in Å) are in parenthesis

	Bulk[a]			Slab[b]	
	$Ni_{1/4}TiS_2$	$Fe_{1/4}TiS_2$		$Ni_{1/4}TiS_2$	$Fe_{1/4}TiS_2$
S_1	−0.41	−0.43	S_1^I	−0.37	−0.40
			S_1^{III}	−0.45	−0.45
S_2	−0.47	−0.52	S_2^I	−0.35	−0.39
			S_2^{III}	−0.50	−0.56
Ti_1	+0.74	+0.73	Ti_1	+0.75	+0.80
Ti_2	+0.85	+0.89	Ti_2	+0.81	+0.84
M	+0.38	+0.58	M	+0.42	+0.78
Ti_2–S_1	0.136 (2.414)	0.134 (2.435)	Ti_2–S_1^{III}	0.136 (2.416)	0.133 (2.421)
			Ti_2–S_1^I	0.132 (2.442)	0.130 (2.440)
Ti_2–S_2	0.123 (2.414)	0.115 (2.435)	Ti_2–S_2^{III}	0.118 (2.405)	0.124 (2.409)
			Ti_2–S_2^I	0.136 (2.407)	0.118 (2.439)
Ti_1–S_2	0.124 (2.414)	0.116 (2.435)	Ti_1–S_2^{III}	0.117 (2.431)	0.086 (2.568)
			$Ti_1 - S_2^I$	0.140 (2.381)	0.169 (2.285)
M–S_2	0.073	0.069	M–S_2^{III}	0.066	0.067

[a] Symbols Ti_1, Ti_2, S_1, S_2 are attached to the $M_{1/4}TiS_2$ bulk. S_2 atoms are coordinated to metal and titanium atoms while the S_1 atoms have only titanium as first neighbors. In all cases Ti_1 is the titanium atom plumbing with metal atom and the Ti_2 atoms are below or above the empty octahedral site of the van der Waals gap.
[b] The symbols S_1^I, S_2^I, Ti_1, Ti_2, S_1^{III}, S_2^{III} refer to the non-equivalent atoms in the slab as defined in Fig. 3.

compounds), the bond between the guest metal atom (Ni or Fe) and one of its first sulfur neighbors has a partially covalent character, as shown by the values of the corresponding bond overlap populations (around 0.07 e^- for the four cases). Then we can conclude that the insertion of the metal atom in the van der Waals gaps leads to the loss of the two-dimensional characteristic of the mother compound TiS_2.

4.2. Analysis of the total electronic density: interpretation of AFM images

At a first approximation, the interpretation of the AFM images needs the analysis of the total electronic density at the outermost surface of the slab. The atomic net charges of the S_1^I and S_2^I atoms resulting from a Mulliken population analysis (Table 1) at the B3LYP level are almost the same, in the two cases (−0.37 e^- and −0.35 e^- in $Ni_{1/4}TiS_2$ and −0.40 e^- and −0.39 e^- in $Fe_{1/4}TiS_2$). Note that for the S_1^I and S_2^I atoms, the repartition of the valence electrons in the 3s, $3p_x$, $3p_y$ and $3p_z$ orbitals reported in Table 2 is very similar both for the two types of sulfur atoms and in the two compounds. In both cases, the top layer sulfur atoms exhibit a specific behavior in comparison with the 3D systems. The net charges of sulfur atoms in the bulk are more differentiated (−0.41 e^- and −0.47 e^- in $Ni_{1/4}TiS_2$ and 0.43 e^- and −0.52 e^- in $Fe_{1/4}TiS_2$). Note that in the slab, the difference between the net charges of S_1^{III} and S_2^{III} atoms is similar to the bulk, which is consistent with a specific behavior of anions from the last atomic plane.

Table 2
Repartition of the valence atomic electron charge (C) of the top layer sulfur atoms into the 3s, $3p_x$, $3p_y$ and $3p_z$ atomic orbitals

	$Ni_{1/4}TiS_2$		$Fe_{1/4}TiS_2$	
	S_1^I	S_2^I	S_1^I	S_2^I
C	6.367	6.351	6.396	6.394
3s	31.2%	31.2%	31.0%	30.9%
$3p_x$	22.8%	23.1%	23.1%	23.2%
$3p_y$	22.8%	23.1%	23.1%	23.2%
$3p_z$	23.0%	22.6%	22.8%	22.6%

Furthermore, the total electron density maps computed in the (1 1 0) plane are reported in Figs. 5(a) and (b) for M = Ni and Fe, respectively. These maps exhibit similar characteristics. They can only be differentiated by the isodensity curves around the guest metal. The spherical behavior of the total electronic density around Ni confirms the

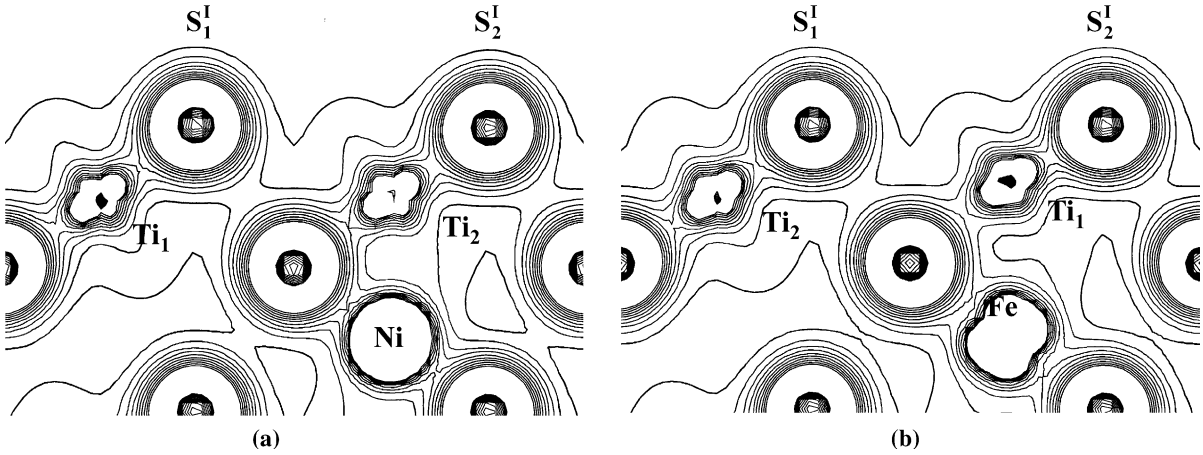

Fig. 5. Total charge density map of the $Ni_{1/4}TiS_2$ (a) and $Fe_{1/4}TiS_2$ (b) slabs plotted for the (1 1 0) plane.

quasi-isotropic distribution of the valence electrons in the 3d orbitals (1.80 e^- for $3d_{z^2}$, 1.81 e^- for $3d_{xz}$ and $3d_{yz}$, 1.85 e^- for $3d_{xy}$ and $3d_{x^2-y^2}$). The distortion observed around the Fe atom can also be related to the electronic populations of the 3d orbitals (1.79 e^- for $3d_{z^2}$, 1.12 e^- for $3d_{xz}$ and $3d_{yz}$, 1.41 e^- for $3d_{xy}$ and $3d_{x^2-y^2}$). Clearly, the nature of the guest specie (Ni or Fe) does not directly affect the total electronic density of the sulfur atoms at the surface of the slab, in contrary to the bulk behavior. This feature associated with slight variations of the sulfur atoms altitudes explain that the AFM images recorded in contact mode exhibit similar characteristics.

However, some interesting differences are noticed when considering the dipole and quadrupole moments of the top layer sulfur atoms along the direction perpendicular to the slab (reported in Table 3). This type of analysis has already been successfully used in the study of LiH [21] or BeO slabs [22]. The atomic multipoles are defined by partitioning the electron charge distribution according to the Mulliken scheme. For a general atom A, the multipole moment $\gamma_A(1,m)$ is defined by

$$\gamma_A(l,m) = \sum_{\mu\in A}\sum_{\nu}\sum_{g} P^g_{\mu\nu}\langle\chi^0_\mu|X^m_l|\chi^g_\nu\rangle,$$

where χ^0_μ and χ^g_ν are the μth and νth atomic orbitals in the cells 0 and g, respectively. X^m_l is the spherical harmonic corresponding to (l,m) quantum numbers and $P^g_{\mu\nu}$ is an element of the first-order density matrix P. The dipole D_z (z; $\gamma_S(1,0)$) and the quadrupole Q_z ($2z^2-x^2-y^2$; $\gamma_S(2,0)$) moments of the top layer atoms permit to compare the deformation of the S_1^I and S_2^I electronic clouds in the normal direction to the slab (Table 3). The dipole moment is taken relative to the nuclear position. In both cases, the top layer sulfur atoms show a positive dipole moment, which corresponds to a displacement of the electron charge towards the interior of the surface. This is consistent with the results obtained from the geometry optimization where the two first planes exhibit a contraction for both compounds. Such a displacement is essentially due to the attraction exerted by the underlying titanium atoms, whose dipole moments D_z are negative, showing an opposite motion of their electron charges towards the slab. The different order of magnitude of D_z for Ti_1 and Ti_2 between $Fe_{1/4}TiS_2$ ($D_z(Ti_1) = -0.196$ a.u. and $D_z(Ti_2) = -0.025$ a.u.) and $Ni_{1/4}TiS_2$ ($D_z(Ti_1) = -0.100$ a.u. and $D_z(Ti_2) = -0.083$ a.u.) could be related to the geometrical optimiza-

Table 3
Total dipole (D_z) and quadrupole moments (Q_z) (in 10^{-3} a.u.) perpendicular to the surface of the top layer sulfur atoms

	$Ni_{1/4}TiS_2$		$Fe_{1/4}TiS_2$	
	S_1^I	S_2^I	S_1^I	S_2^I
D_z	+95.15	79.17	+70.85	+74.47
Q_z	−204.00	−32.42	−115.40	+48.15

tion (Fig. 4) of the corresponding atoms for the two inserted compounds.

For $Ni_{1/4}TiS_2$, the S_2^I dipole moment (0.079 a.u.) is smaller than the S_1^I one (0.095 a.u.) by 18%. On the other hand, for $Fe_{1/4}TiS_2$, the dipole moments of the two types of sulfur atoms (0.071 and 0.074 a.u. for S_1^I and S_2^I, respectively) are almost the same and of the same order of magnitude as the S_2^I one in $Ni_{1/4}TiS_2$. Note that whatever the considered sulfur atoms, the D_z component is the most important one of the total dipole moment $\vec{\mathbf{D}}$. For the S_1^I atoms, $\vec{\mathbf{D}}$ is directed along the z direction, the other components being equal to zero. For the S_2^I type of atom, D_z represents 99.2% and 99.9% of D for M = Fe and M = Ni, respectively, leading to respective angles of 7° and 3° between $\vec{\mathbf{D}}$ and the Oz direction. Besides these small displacements of the electron charges, the deformation occurring in the shape of the electron distribution are quantified by the quadrupole moment. The negative values of the quadrupole moment component perpendicular to the slab for the S_1^I atoms in the two compounds imply an elongation undergone by their electron clouds in this direction. The S_1^I quadrupole moment is two times smaller in $Fe_{1/4}TiS_2$ (−0.115 a.u.) than in $Ni_{1/4}TiS_2$ (−0.204 a.u.) indicating that the deformation of the electron cloud for this type of atom is more important in the Ni case. The S_2^I atoms are less affected by this type of deformation. They undergo a slight squeezing in the z direction and in the xOy plane, respectively, for $Ni_{1/4}TiS_2$ ($Q_z = -0.032$ a.u.) and $Fe_{1/4}TiS_2$ ($Q_z = +0.048$ a.u.), in agreement with a shorter distance Ti_1–S_2^I in $Fe_{1/4}\ TiS_2$.

All these modifications of the electronic behavior highlighted by the multipolar analysis are not revealed by repulsive forces detection (contact AFM). The tip to surface interaction is too strong (even if the force applied to the tip was the lower as possible to detect such differences).

4.3. Analysis of the electronic density $\Delta E = 0.3$ eV above the Fermi level E_F: interpretation of the STM image

The vertical coordinates of the S_1^I and S_2^I atoms are quasi the same, implying, in the interpretation of the STM image of $Fe_{1/4}TiS_2$, an almost negligible influence of the geometrical factor originating from the exponential decrease of atomic amplitude with distance, On the contrary, for $Ni_{1/4}TiS_2$, the geometrical factor contributes to the differentiation between the two types of sulfur atoms suggesting more luminosity for S_1^I atoms on the STM image. However, it is still necessary to consider the electronic factor by analyzing the electronic density $\rho(r, E_F)$ at the Fermi level (in practice, 0.3 eV below E_F), for both compounds.

The projected DOS in the interval $[E_F - 0.3, E_F]$ corresponding to each type of top sulfur atoms in $Ni_{1/4}TiS_2$ and $Fe_{1/4}TiS_2$ (slab and bulk) are reported in Fig. 6. For both systems in the slabs, the S_1^I contribution to electronic density below E_F is higher than the S_2^I one (Figs. 6(a) and (c)). In this energy interval, the integrated densities for the projected DOS (Table 4) show that these two types of sulfur atoms are less differentiated for M = Fe than M = Ni. This difference is essentially due to the predominant p_z character of the S_1^I density in the last filled bands (63% for M = Fe and 75% for M = Ni). However, for M = Fe, the S_2^I density exhibits also an important p_z character (58%), but weaker than for the S_1^I atom. For M = Ni, the participation of p_z to the S_2^I density is reduced to 46%, the p_y (or p_x) one being equal to 31%.

On the other hand, for the 3D systems, the two curves (Figs. 6(b) and (d)) representing the projected DOS for each type of sulfur atom are nearly the same and the two types of sulfur atoms (S_2 and S_1) cannot be differentiated by their respective contribution to the electronic density around the Fermi level.

Furthermore, the electron charge density maps implemented in the interval $[E_F - 0.3, E_F]$ and projected in the (1 1 0) plane for both compounds (Figs. 7(a) and (b)) confirm these features. The predominant p_z character of the S_1^I density is confirmed in both cases. Moreover, the difference between the two compounds in the directional effect relative to the S_2^I top layer atoms appears very clearly. These maps underline the differences observed for the contribution of titanium sublayer atoms to $\rho(r, E_F)$. Particularly, the contribution of Ti_1 atoms is completely different. In $Fe_{1/4}TiS_2$, the electronic density of Ti_1 atom (0.10 e^-) has an

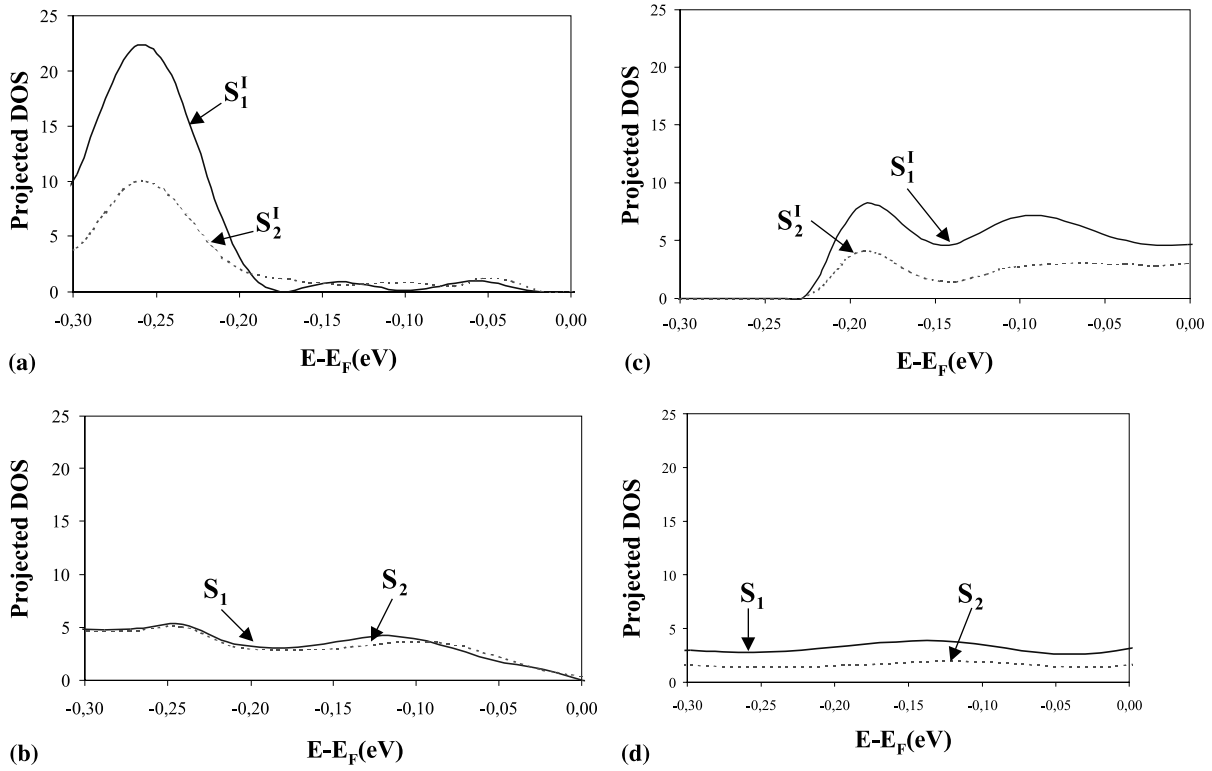

Fig. 6. Projected DOS plotted in the energetic window $[E_F - 0.3\ \text{eV}, E_F]$: (a) for the top layers S_1^I and S_2^I sulfur atoms in the $Ni_{1/4}TiS_2$ slab; (b) for the S_1 and S_2 sulfur atoms in the $Ni_{1/4}TiS_2$ bulk; (c) for the top layers S_1^I and S_2^I sulfur atoms in the $Fe_{1/4}TiS_2$ slab; (d) for the S_1 and S_2 sulfur atoms in the $Fe_{1/4}TiS_2$ bulk.

Table 4
Integrated densities of the atomic projected DOS in the interval $[E_F - 0.3, E_F]$ for the slabs

	$Fe_{1/4}TiS_2$	$Ni_{1/4}TiS_2$
S_1^I	0.05	0.07
S_2^I	0.02	0.03
Ti_1	0.10	0.05
Ti_2	0.22	0.06
S_1^{III}	0.01	0.02
S_2^{III}	0.01	0.04
M	0.19	0.61

important d_{z^2} character (45%). The contribution of these atoms in $Ni_{1/4}TiS_2$ is two times lower than for M = Fe and corresponds to an hybridization dominated by the $3d_{xz}$ and $3d_{yz}$ orbitals (32%). Consequently, the interactions Ti_1–S_2^I are different according to the nature of the inserted specie, leading to a more important indirect contribution of the Ti_1 atoms to the electronic density detected by the tip at the S_2^I atom, for M = Fe.

The study of the atomic dipole $D_z(E_F)$ computed in the interval $[E_F - 0.3, E_F]$ permits to refine the analysis of $\rho(r, E_F)$. In both compounds, the top layer sulfur dipoles are negative, corresponding to a displacement of the electron charge towards the exterior of the surface and an elongation of the corresponding electron clouds. This $D_z(E_F)$ orientation at the Fermi level opposite to the one previously reported for the total dipole moments confirms the specific behavior (antibonding) of the electrons in the last filled bands compared to those of the valence bands. In both cases the S_1^I dipole moments (−0.0739 and −0.0703 a.u. for M = Ni and Fe, respectively) which are greater than the S_2^I ones underline also the predominant z character of the S_1^I electronic density. The values of the S_2^I dipole moment (−0.0303 and −0.0142 a.u. for

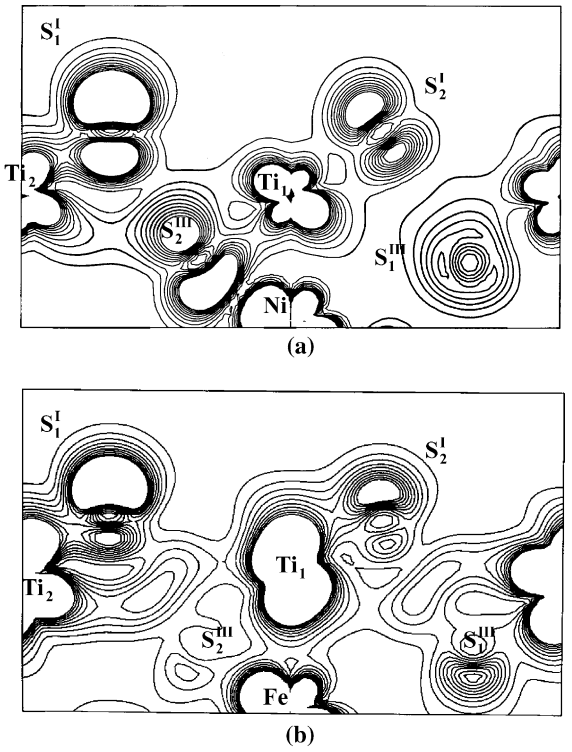

Fig. 7. $[E_F - 0.3\ \text{eV}, E_F]$ charge density map of the $Ni_{1/4}TiS_2$ (a) and $Fe_{1/4}TiS_2$ (b) slabs plotted for the (1 1 0) plane.

M = Fe and M = Ni, respectively) confirm that the electronic density detected by the tip for these atoms is more important for $Fe_{1/4}TiS_2$, which minimize the differentiation between the types of sulfur atoms for this material. Note that the relatively important value of the Ti_1 quadrupole moment in $Fe_{1/4}TiS_2$ (−0.039 a.u.) compared to this in $Ni_{1/4}TiS_2$ (+0.0002 a.u.) confirms the (indirect) participation of these atoms to the electronic density detected by the tip at the S_2^I atom for M = Fe. It is clearly highlighted by the electronic charge density maps projected in the (1 1 0) plane for M = Fe (Fig. 7(b)), confirming the elongation of the corresponding electron cloud in the z direction and influencing S_2^I atoms.

Then, for $Fe_{1/4}TiS_2$, we have shown that the nature of the interaction Ti_1–S_2^I in the interval $\Delta E = 0.3$ eV below the Fermi level reduces considerably the differentiation of the S_1^I and S_2^I atoms. The electronic density detected by the tip at the S_2^I level is increased by the participation of the $d_{z^2}(Ti_1)$ orbitals. The geometrical optimization is essential to traduce the influence of the interaction Ti_1–S_2^I (the distance between these atoms is reduced by 0.15 Å by the surface relaxation). However, it is not possible to distinguish brightness

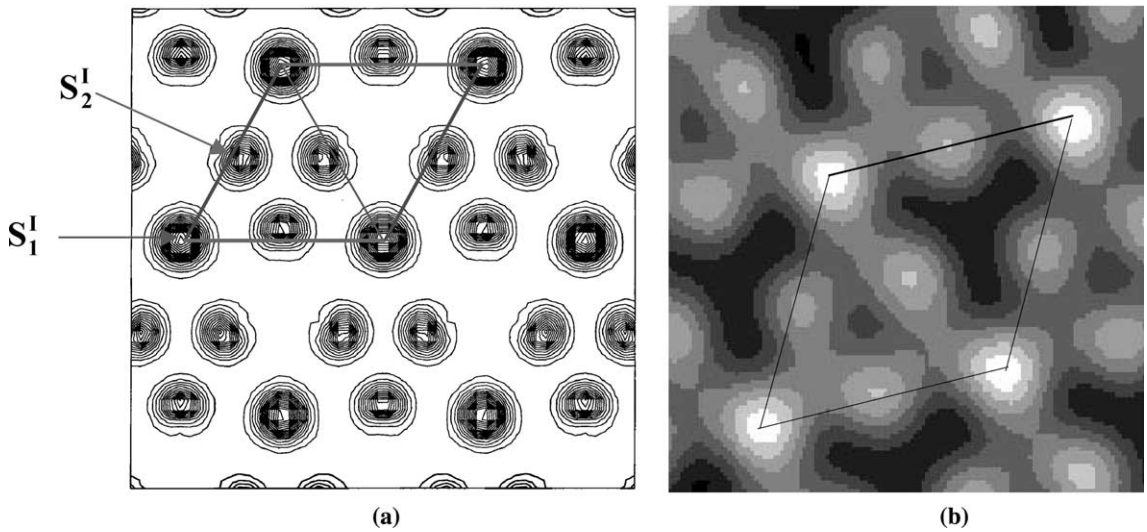

Fig. 8. $[E_F - 0.3\ \text{eV}, E_F]$ charge density map plotted for the (1 1 0) plane, 0.5 Å above the top sulfur layer of the $Ni_{1/4}TiS_2$ slab (a). The $Ni_{1/4}TiS_2$ map is compared to the experimental zoomed STM image (b).

differences due to electronic densities variations detected by the tip even if the S_1^I electronic density appear slightly more important than the S_2^I one, in accordance with the previous analysis of the projected atomic DOS.

For $Ni_{1/4}TiS_2$, both geometrical and electronic factors contribute to differentiate the S_1^I and S_2^I atoms in accordance with the STM image. To simulate the STM images, the electron density maps in the (0 0 1) plane, 0.5 Å above the top sulfur layer, are computed around the Fermi level (see Fig. 8(a)). As expected, the differentiated S_1^I and S_2^I atoms (both geometrically and electronically) correspond respectively to the bright and dark spots observed on the image of $Ni_{1/4}TiS_2$ (Fig. 8(b)). Furthermore, the two triangular zones with different brightness are clearly identified and as in the STM image three S_1^I sulfur atoms delimit each of them.

5. Conclusion

A biperiodical approach within the periodic LCAO-B3LYP approximation was necessary to account for the STM and AFM images of $Mi_{1/4}TiS_2$ (M = Fe, Ni) surface compounds. Both experimental results obtained from different probes were interpreted on the basis of the partial electron density $\rho(r, E_F)$-STM – and total electron density $\rho(r)$-AFM – of a slab which consists of seven (0 0 1) $M_{1/4}TiS_2$ atomic layers.

The same sulfur hexagonal lattices revealed by atomic force microscopy data for Fe and $Ni_{1/4}TiS_2$ are consistent with the total electron density maps computed in the (1 1 0) plane to visualize the electronic contribution of each chalcogen atoms. However, some interesting differences concerning the top sulfur layers were highlighted by both the geometrical optimization and the multipolar analysis. A specific behavior of sulfur atoms from the slab compared to the bulk ones is shown.

The differentiation of the two types of sulfur atoms evidenced experimentally by STM analysis on $Ni_{1/4}TiS_2$ was explained in terms of different directional electronic contributions at the Fermi level (density of states, z dipole and quadripole moments) and geometrical factors. The order of magnitude of these differences are clearly lower for $Fe_{1/4}TiS_2$; the titanium subsurface atoms appears responsible via the inserted species (Fe) to the reduction of the brightness differences detected by the tip.

The model used seems suitable in this case to interpret both STM and AFM images. This work shows the necessary complement between both experimental and theoretical approaches to understand accurately the surface electronic structures of these compounds.

References

[1] J. Rouxel, in: F.A. Lévy (Ed.), Intercalated Layered Materials, P201, Reidel Publishing Compagny, Dordrecht-Holland/Bostan-USA, 1979.
[2] M.S. Whittinghan, Prog. Solid State Chem. 12 (1978) 41.
[3] (a) M. Inoue, H.P. Hughes, A.D. Yoffe, Adv. Phys. 5 (1989) 565;
(b) M. Inoue, M. Koyano, H. Negishi, Y. Veda, J. Phys. Soc. Jpn. 55 (1986) 1400.
[4] H. Negishi, S. Ohara, Y. Takata, T. Yokoyama, M. Tarriguchi, M. Inoue, Mater. Sci. Forum 91–93 (1992) 603.
[5] M.H. Whangbo, J. Rouxel, L. Trichet, Inorg. Chem 24 (1985) 1824.
[6] H. Martinez, Y. Tison, I. Baraille, M. Loudet, D. Gonbeau, J. Electron Spectrosc. Related Phenom. 125 (3) (2002) 181.
[7] R. Dovesi, V.R. Saunders, C. Roetti, M. Causà, N. Harrison, R. Orlando, E. Aprà, CRYSTAL 98 User's Manual, Università di Torino, Torino, 1996.
[8] C. Pisani, R. Dovesi, C. Roetti, in: Hartree–Fock Ab Initio Treatment of Crystalline Solids, Lecture Notes in Chemistry, vol. 48, Springer, Heidelberg, 1988.
[9] G.V. Subba Rao, M.W. Shafer, L. Tao, Mater. Res. Bull. 8 (1973) 1231.
[10] I. Baraille, H. Martinez, Y. Tison, D. Gonbeau, M. Loudet, Surf. Sci. 517 (2002) 43.
[11] A.D. Becke, J. Chem. Phys. 98 (1993) 5648.
[12] C. Lee, W. Yang, R.G. Parr, Phys. Rev. B 37 (1988) 785.
[13] P. Durand, J.C. Barthelat, Theor. Chem. Acta 38 (1975) 283.
[14] B. Silvi, N. Fourati, R. Nada, C. Catlow, J. Phys. Chem. Solids 52 (1991) 1005.
[15] Y. Bouteiller, C. Mijoule, M. Nizam, J.C. Barthelat, J.P. Daudey, M. Pelissier, B. Silvi, Mol. Phys. 65 (1988) 295.
[16] T. Ouazzani, A. Lichanot, C. Pisani, C. Roetti, J. Phys. Chem. Solids 54 (1993) 1603.
[17] PENTE, A. Dargelos, Laboratoire de Chimie Théorique et de Physico-Chimie Moléculaire, UMR CNRS 5624, 1999.
[18] M. Inoue, H. Negishi, J. Phys. Chem. 90 (1986) 235.
[19] S.N. Magonov, M.H. Whangboo, Adv. Mater. 6 (1994) 355.
[20] H. Martinez, P. Azavant, M. Loudet, Surf. Sci. 400 (1998) 247.
[21] M. Causà, R. Dovesi, F. Ricca, Surf. Sci. 237 (1990) 312.
[22] A. Lichanot, I. Baraille, C. Larrieu, M. Chaillet, Phys. Rev. B 52 (1995) 17480.